



Application and assessment of a GPU-based LES method for predicting dynamic wind loads on buildings

Bálint Papp^{a,*}, Gergely Kristóf^a, Christof Gromke^b

^a Department of Fluid Mechanics, Faculty of Mechanical Engineering, Budapest University of Technology and Economics, Műegyetem rkp. 3, 1111, Budapest, Hungary

^b Laboratory of Building and Environmental Aerodynamics, Institute for Hydromechanics, Karlsruhe Institute of Technology, Kaiserstr. 12, 76133, Karlsruhe, Germany

ARTICLE INFO

Keywords:

Dynamic wind load
Cube surface pressure
Wind tunnel experiment
Large Eddy Simulation (LES)
Graphics processing unit (GPU)

ABSTRACT

This study presents the assessment of a fast Large Eddy Simulation method for estimating dynamic wind loads on buildings using a GPU-based CFD software, which produces statistically converged results on a nine-million-cell mesh in approximately 6 hours. The surface pressure distribution of a cuboid building model was validated with experimental data obtained in an atmospheric boundary layer wind tunnel and compared with field measurements. Although due to the applied equidistant Cartesian grid the large gradients near the edges are not fully resolved, good overall agreement was found for the mean and fluctuating pressure distributions (correlation coefficient: 0.90/0.73, FAC2: 0.92/0.98, FB: $-/0.06$, MG: $-/0.95$, NMSE: $-/0.10$, VG: $-/1.08$). It was shown that the numerical model is able to produce matching turbulent spectra in an intermediate frequency range within the inertial subrange, limited by the domain size and the spatial resolution. Mesh refinement for capturing large gradients as well as for expanding the frequency limits can be achieved by using a GPU with higher VRAM capacity for the simulation. The continuing advancement of the presented model is a promising development for estimating dynamic wind loads on buildings and identifying design problems fast enough for the engineering practice, without high-performance computing.

1. Introduction

Nowadays, CFD models are accepted tools for assisting building construction and urban design. Model-based analysis is commonly used for studying and predicting air quality, wind comfort, and other urban climate parameters. Such models can accurately take the geometric features of the built environment as well as the interaction between buildings into account. The EUROCODE and AIJ standards (EN, 1991-1-4:2005, Tamura et al., 2008) both accept properly validated Computational Fluid Dynamics (CFD) simulations in combination with wind tunnel tests for the determination of the mean and fluctuating wind loads on built structures. The AIJ guide, for example, allows for the determination of pressure coefficients based on Large Eddy Simulation, whereas the EUROCODE only accepts the CFD-based assessment of wind loads in combination with wind tunnel tests. The history of Computational Wind Engineering and the literature of urban CFD studies is comprehensively reviewed by Blocken (2014, 2015).

Transient wind loads may be the input for both analytical and numerical dynamic vibration analyses of built structures, such as in the studies of Huang et al. (1996), Qu et al. (2001), Xia et al. (2008), Keyhan

et al. (2013), and Domaneschi et al. (2015). Most bridges and high-rise buildings are susceptible to wind excitation; however, they can vibrate vigorously only in a narrow frequency range, so the most critical issue in terms of dynamic wind load is how much of the mechanical excitation energy falls within the frequency range where the mechanical admittance of the structure is significant. The basis of the investigation can be the power spectrum of the surface forces determined by a transient measurement or CFD simulation; hence, the spectral distribution can be considered as an essential model result. The upper frequency limit of a numerical analysis is determined by the spatial and temporal resolution of the numerical model: spectral information can only be provided by models in the resolved range of turbulence, meaning that the numerical mesh behaves as a low pass filter (Tamura, 2009). Moreover, the domain size places a lower limit on the resolved frequency range.

The currently known CFD simulation methods for dynamic wind loads have not yet achieved acceptable speed combined with sufficient accuracy for the engineering practice. The difficulties of transient flow analysis lie in the *computational demand* of scale-resolving turbulence models – such as Large Eddy Simulation (LES), Detached Eddy Simulation (DES), Scale-Adaptive Simulation (SAS), or Stress-Blended Eddy

* Corresponding author.

E-mail address: papp@ara.bme.hu (B. Papp).

<https://doi.org/10.1016/j.jweia.2021.104739>

Received 18 December 2020; Received in revised form 21 July 2021; Accepted 27 July 2021

Available online 9 August 2021

0167-6105/© 2021 The Authors.

Published by Elsevier Ltd.

This is an open access article under the CC BY-NC-ND license

(<http://creativecommons.org/licenses/by-nc-nd/4.0/>).

Simulation (SBES), see [Menter \(2012\)](#) – as well as in the *uncertainties of inflow generation*.

For the turbulent motion to be resolved in time to a satisfactory level of detail, the time step should be limited to around the ratio of spatial resolution and the characteristic velocity; that is, the Courant number should be around unity. On the other hand, the duration of the numerical simulation must be long enough to achieve a developed turbulent flow and to produce statistically converged results. This involves computing times of the scale-resolving CFD models two orders of magnitude larger than those of the standard Reynolds averaged (RANS) turbulence models. The typical time required for the transient CFD analysis of a single building configuration for one wind direction can be measured in weeks or months using a typical engineering workstation. RANS and LES turbulence models are compared critically by [Blocken \(2018\)](#).

A possible cost-effective solution for the acceleration of scale resolving numerical models is the use of a graphics processing unit (GPU) based computer architecture. Powerful GPUs feature several thousand computing cores, imposing high demands on the parallel efficiency of the numerical methods, however, the available graphics memory of the GPU (VRAM) is still limited: it is more expensive and cannot be expanded in a flexible way such as the CPU-managed RAM. The unique features of the new hardware also require different modeling approaches and software implementation, which follow the development of the hardware with several years of delay.

[Elsen et al. \(2008\)](#) implemented the lattice-Boltzmann method on GPU in order to simulate supersonic flows by solving the compressible Euler equations. The maximum speed-up compared to a dual-core CPU was around 40 times for a single airfoil and around 15 times for a full supersonic aircraft geometry, cruising at Mach 5 (which was something out of the reach of previous CFD studies on GPU). [Phillips et al. \(2009\)](#) elaborated and verified a CUDA-based (Compute Unified Device Architecture) solver for the compressible 2D Euler equations, running on a cluster of 16 graphics cards, resulting in an 88 times acceleration over a single CPU and a six times acceleration compared to 16 CPUs. [Thibault and Senocak \(2009\)](#) described the implementation of a 3D Navier-Stokes solver for incompressible fluid flows using desktop platforms equipped with multi-GPUs, achieving speed-ups of 13 and 21 times relative to a single-core and a dual-core CPU, respectively. [Corrigan et al. \(2011\)](#) ran their unstructured grid-based CFD solver on 3D supersonic airfoil and missile models, resulting in roughly 9.5 times and 33 times acceleration over quad-core parallel and serial CPU-based solvers. The above methods building on CUDA, introduced by Nvidia Corporation in 2007, a parallel computing platform and application programming interface (API) which solved several previous limitations of parallel computation. Studies in the field of general-purpose computation on graphics hardware (using GPGPUs) predating the release mentioned above are surveyed by [Owens et al. \(2007\)](#).

The benefits of massive parallelization, such as the reasonable computational time even in the case of outstanding model resolution, were utilized in micrometeorology and wind engineering as well. [Schalkwijk et al. \(2012\)](#) investigated the cloud formation process using an LES-based microscale meteorological model adapted for GPU. The simulation running on a 512-core graphics card was able to reduce the computational time by a factor of nine compared to a single CPU. Moreover, [Onodera et al., 2013](#) investigated the flow field of a 10 by 10 km area of Tokyo, using lattice-Boltzmann-based LES. The 1-m grid resolution applied in their model was able to capture the complex urban flow field in unprecedented detail. In recent years, [King et al. \(2017\)](#) carried out simulations of the external and internal flow conditions of a hollow cube and an array of cuboid building models subjected to an atmospheric boundary layer. By using the lattice-Boltzmann method and an LES-based solver running on a high-performance computation facility, an acceleration of several orders of magnitude was observed compared to the performance of a finite volume-based LES approach on a 16-core CPU-based workstation. The time-averaged and fluctuating

components of the pressure distributions of the transient simulations showed acceptable correspondence with the results by an accepted conventional multipurpose CFD solver and previous experimental data. Finally, the previous work of the authors – applying the same numerical model as in the present paper – investigated the micro-scale urban dispersion of traffic-induced air pollutants with the application of GPU-based Large Eddy Simulation ([Kristóf and Papp, 2018](#)). Excellent agreement was found between the simulation and the experimental results for the concentration distribution of a finite length street canyon exposed to perpendicular wind.

Besides the massive computational demand, another problem about scale-resolving numerical simulations is the definition of a proper inlet boundary condition. The methods used for setting up the inlet conditions carry uncertainty both for wind tunnel tests as well as for numerical models. The mean velocity and turbulence profiles achieved in various wind tunnel measurements vary considerably, so the experimental results are also scattered ([Hölscher and Niemann, 1998](#); [Thordal et al., 2019](#), and the references therein). In the case of Reynolds-averaged models, the proper specification of turbulent characteristics causes difficulties ([Richards and Hoxey, 1993](#); [Blocken et al., 2007](#); [Richards and Norris, 2011](#); [Balogh et al., 2012](#)). The turbulence profiles used for defining inlet conditions must be consistent with the applied turbulence model, without which the velocity profile rapidly degenerates. Scale-resolving (transient) numerical models either follow the geometric design of wind tunnels or artificially synthesize turbulence at the inlet boundary ([Thordal et al., 2019](#)). The so-called precursor simulation approach described by [Spalart and Leonard \(1987\)](#), [Lund et al. \(1998\)](#), [Kataoka and Mizuno \(2002\)](#), and further developed by [Nozawa and Tamura \(2002\)](#) and [Xie and Castro \(2008\)](#), as well as [Kim et al. \(2013\)](#) uses a streamwise periodic domain and decomposes the outlet velocity into mean and fluctuating components, the latter of which is superimposed to a prescribed mean velocity profile at the upstream boundary. The advantage of the synthetic turbulence generation approach is that the domain size can be significantly reduced. On the other hand, synthetic turbulence has a structure and behavior different from natural or wind tunnel turbulence, which causes a more significant uncertainty in the model results. [Lim et al. \(2009\)](#), [Dagnew and Bit-suamlak, 2014](#), [Aboshosha et al. \(2015\)](#), [Patruno et al. \(2016\)](#), [Ricci et al. \(2018\)](#) as well as [Lamberti and Gorlé \(2020\)](#) investigated the transient wind load of buildings using LES, concluding that the good agreement of the numerical results with experimental data is strongly dependent on the specified inflow conditions, such as the main parameters of the incoming atmospheric boundary layer.

In the framework of the present study, wind tunnel experiments were performed with a cube-shaped building model in a simulated urban boundary layer to determine the time-dependent surface pressure distribution; moreover, GPU-based LES calculations were run using a unique method for generating an urban-like boundary layer. The simulated and measured surface distributions of the pressure coefficient are compared for the cubic building model aligned with the flow and rotated by 45°. Based on the transient surface pressure distributions of the building, the structural loads can be calculated. In this paper, the time-averaged mean and standard deviation results, as well as power spectra are compared. The CFD model is further compared against the mean surface pressure coefficients provided by previous wind tunnel tests and the Silsoe field experiments ([Hölscher and Niemann, 1998](#); [Richards et al., 2001](#); [Richards and Hoxey, 2012](#)).

2. Materials and methods

2.1. Wind tunnel setup and measurements

2.1.1. Wind tunnel and approach flow

The measurements were performed in an atmospheric boundary layer wind tunnel at the Laboratory of Building and Environmental Aerodynamics at the Karlsruhe Institute of Technology (KIT). The

boundary layer wind tunnel has a cross-section of 2 m by 1 m (width by height) with a precisely adjustable ceiling in the test section, comprising 16 segments, each of 47 cm length, to enable a flow with vanishing pressure gradient in streamwise direction ($dp/dx = 0$). Flow conditioning is achieved by means of flow straighteners followed by Irwin-type vortex generators, a horizontally ground-mounted tripping device, and a subsequent fetch of 6 m length covered with roughness elements, see Fig. 1. In the test section, an adequately developed simulated atmospheric boundary layer flow is reproduced. The vertical profile of the mean streamwise velocity $u(z)$ can be described by a power-law formulation according to

$$\left(\frac{u(z)}{u_{ref}}\right) = \left(\frac{z}{z_{ref}}\right)^{\alpha_u}, \quad (1)$$

with reference height z_{ref} , reference velocity u_{ref} , and profile exponent $\alpha_u = 0.30$. Hence, the simulated flow represents atmospheric boundary layer flows typical for urban environments, see, e.g., the German wind code and its national appendix (DIN EN 1991-1-4, 2010; DIN EN 1991-1-4/NA, 2010) or the VDI guideline for environmental meteorology (VDI 3783-12, 2000). In the present study, the free-stream velocity at the boundary layer top was set to $u_s = 7$ m/s, the reference height chosen to $z_{ref} = 0.1$ m, and a value of 4.39 m/s for u_{ref} was obtained. For more comprehensive information on the simulated atmospheric boundary layer flow, its development (homogeneity) in the streamwise and lateral direction, data about the turbulence intensity profile $I_u(z)$, the integral length scale profile $L_{ux}(z)$, and spectral distribution of turbulent kinetic energy $S_{uu}(z,f)$, the reader is referred to Gromke and Ruck (2005).

2.1.2. Cube/building model

In the center of the test section of the wind tunnel, a cube with an edge length of $L = 0.2$ m was placed on a turntable. The walls of the cube were made of acrylic glass (PMMA), which allowed the building model to have distinctly smooth surfaces and well-defined sharp edges. One face of the cube was equipped with 35 pressure measurement taps made of flush-mounted brass tubes with an inner diameter of 1 mm (Fig. 2).

The Reynolds number based on the cube edge length L and the undisturbed approach flow velocity at cube top $u_L = u(L) = 5.40$ m/s is calculated to $Re_L = 72,000$. Thus, the threshold Reynolds number of 15,000 – above which in bluff body aerodynamics the flow field is considered to be Re-insensitive (see Gromke (2018) and the references

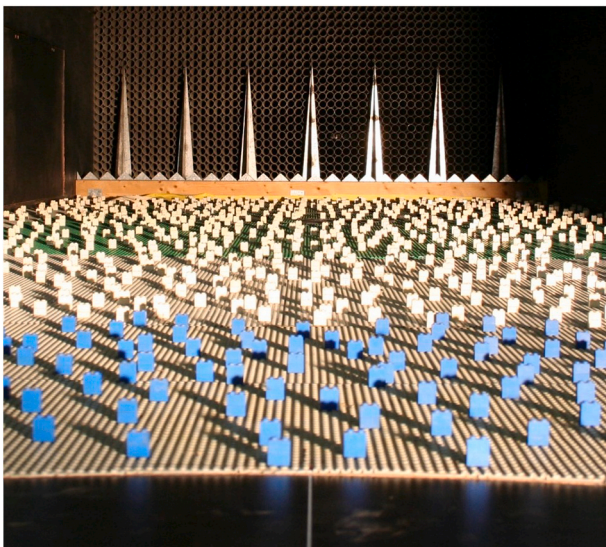


Fig. 1. Flow conditioning section in the atmospheric boundary layer wind tunnel at the Laboratory of Building and Environmental Aerodynamics at Karlsruhe Institute of Technology (KIT).

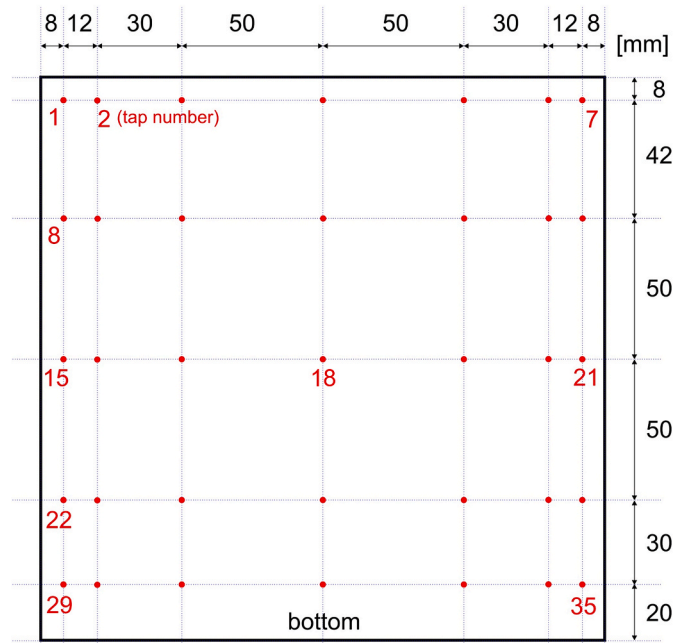
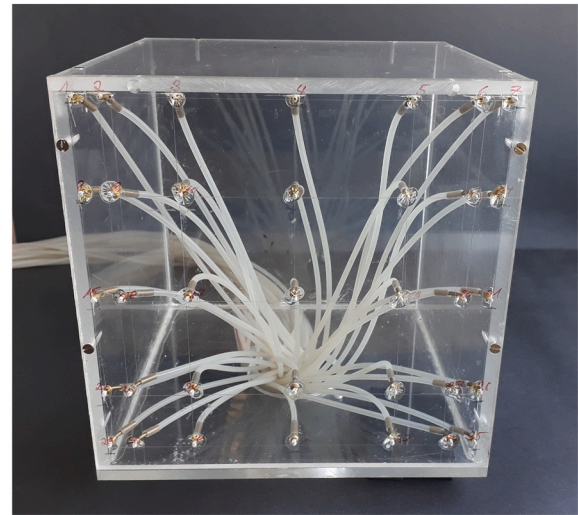


Fig. 2. The acrylic glass cube and the positions of the pressure measurement taps.

therein –), as well as the critical Reynolds number of 50,000 – above which Költzsch et al. (1997) found a Re-insensitive pressure distribution at the roof of a sharp-edged cube – are both clearly exceeded.

2.1.3. Pressure measurements and signal processing

The pressure measurements were performed with two miniature pressure scanners (type ESP-32HD), providing a total of 64 silicon piezoresistive differential pressure transducers and recorded by a data acquisition system (type DTC Initium), both from PSI Pressure Systems. The transducers span a pressure range of ± 25 mbar (2500 Pa), and their analog output signals were A/D converted with a sampling frequency of $f_s = 500$ Hz and 18-bit resolution for an acquisition time of $t_{ac} = 120$ s obtained by one measurement record. Given the integral time scale $T_{lux} = 0.025$ s in the height layer of the cube (Gromke and Ruck, 2005), the acquisition time encompasses 4800 passages of the largest eddy structures.

The static accuracy of the pressure transducers, including combined errors due to non-linearity, hysteresis, and non-repeatability is specified

Table 1
Definitions for the different surface pressure coefficients used in this paper.

Name	Notation	Formula	Normalized by	Relevance
Mean pressure coefficient	c_p	$\frac{\text{Mean}(p(t) - p_0)}{0.5\rho u_L^2}$	Mean dynamic pressure at cube height	Sections 3.1, 3.3 and 3.4
Fluctuating pressure coefficient	c_p'	$\frac{\text{StDev}(p(t) - p_0)}{0.5\rho u_L^2}$	Mean dynamic pressure at cube height	Section 3.1
Standard deviation pressure coefficient	\bar{c}_p	$\frac{\text{StDev}(p(t) - p_0)}{\text{StDev}(0.5\rho u_L^2(t))}$	Standard deviation of the dynamic pressure at cube height (Richards and Hoxey, 2012)	Section 3.3

In the above formulas, $p(t)$ is the static pressure time series at the cube surface, p_0 is the reference mean static pressure, ρ is the air density, u_L is the streamwise reference mean velocity, taken from Eq. (1) at cube height $z = L$, and $u_L(t)$ is the streamwise pressure time series corresponding to $z = L$ (with its time-average being equal to u_L). $\text{Mean}(x(t))$ and $\text{StDev}(x(t))$ denote the mean and standard deviation of the time series $x(t)$, respectively.

to a maximum of 0.1% FSO (FSO: Full-Scale Output) by the manufacturer. Furthermore, the thermal error of the transducers is given as 0.004% FSO/°C with reference to $t_{ref} = 22$ °C, and the resolution error of the DAQ device is specified as 0.003% FSO. Assuming a maximum temperature deviation of $\Delta T = 5$ °C relative to the reference temperature $t_{ref} = 22$ °C, the total error can be estimated to be less than $\delta_p = 2.55$ Pa according to the law of propagation of uncertainties.

The pressure taps at the cube surface were connected by 1.20 m long silicone tubes with an inner diameter of 1 mm to the pressure transducer. No restrictors in the tubing system were used. Instead, a transfer function (Bergh and Tijdeman, 1965) was applied to correct for frequency-dependent amplitude damping and phase shift distortions. The signal processing was implemented in a MATLAB script, which further involved low-pass filtering before the pressure coefficients were determined according to the formulas in Table 1. Besides analyzing the distribution of the mean pressure coefficient (c_p), the fluctuating pressure coefficient (c_p') can be used to relate the magnitude of the surface pressure variance to the time-averaged values (Section 3.1). Moreover, the standard deviation pressure coefficient (\bar{c}_p) is calculated following the definition by Richards and Hoxey (2012) in order to compare the results of the present study to full-scale experimental data (Section 3.3).

For the filtering, a 10th-order infinite impulse response (IIR) low-pass digital Butterworth filter with a cut-off frequency of $f_{co} = 50$ Hz was employed. This cut-off frequency was chosen because the visual inspection of the power spectral density of unfiltered measurement signals revealed only negligibly small contributions for $f > 50$ Hz, which are attributable to noise rather than to an actual energy (power) content. The apparent main effect of the filter was to remove outliers from the time series of the measurement signal.

Prior to the measurements, the offset of each pressure transducers was determined in a zero-pressure environment acquisition. The reference pressure (p_0) was taken from a static pressure measurement tap at a sidewise wind tunnel wall with undisturbed parallel flow conditions, at the center of the cube in streamwise direction, and at 25 cm (1.25 L) above the wind tunnel floor.

2.2. CFD model and simulations

2.2.1. Computational domain and boundary conditions

The numerical model – shown in Fig. 3 – was created in ANSYS Discovery Live 2019R3, which is designed to perform high-speed Large Eddy Simulation utilizing the parallel computing capabilities of the GPU architecture. The numerical wind tunnel was designed to replicate the wind tunnel setup and flow characteristics described in the above section and was previously introduced and validated for dispersion by Kristóf and Papp (2018). It has a streamwise length (relative to the cube edge length L) of $18L$, a lateral width of $9.6L$, and a height of $3L$. The frontal face of the cube is located at $11.4L$ distance from the inlet plane. The dimensions of the numerical wind tunnel are different from the standard layouts commonly employed in RANS CFD (Franke et al., 2007; Tominaga et al., 2008); however, the differences in the domain size are consequences of a trade-off, which had to be made for a sufficiently fine spatial resolution. It is important to note that although the height of the simulation domain is smaller than the recommended value in the guidelines, the maximum change in the streamwise velocity was 3.3% (at the top of the domain at a streamwise line at $y/H = 0$) compared to the empty simulation domain. The blockage ratio in the investigated case is 3.4%, which is an acceptable value in wind tunnel experiments.

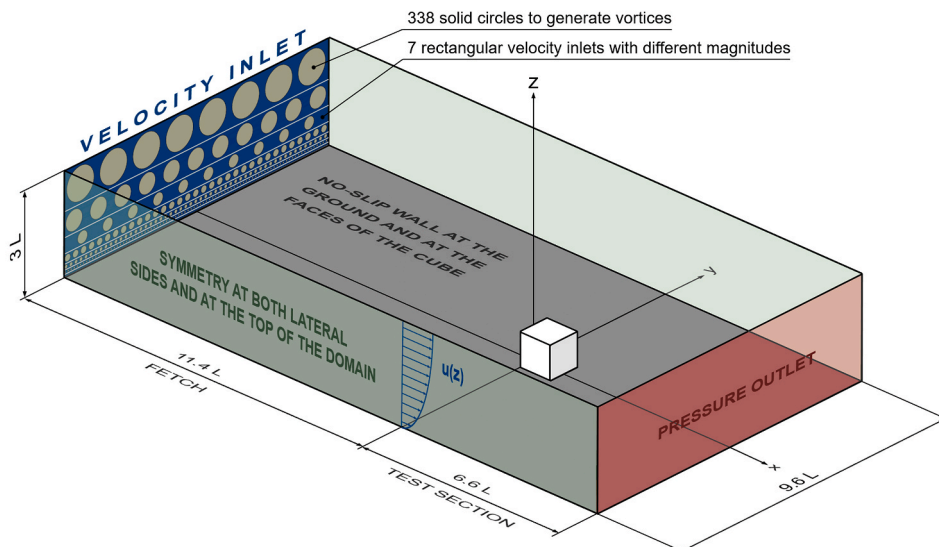


Fig. 3. Geometrical dimensions and boundary conditions of the GPU-based numerical wind tunnel. The cube edge length is $L = 20$ cm.

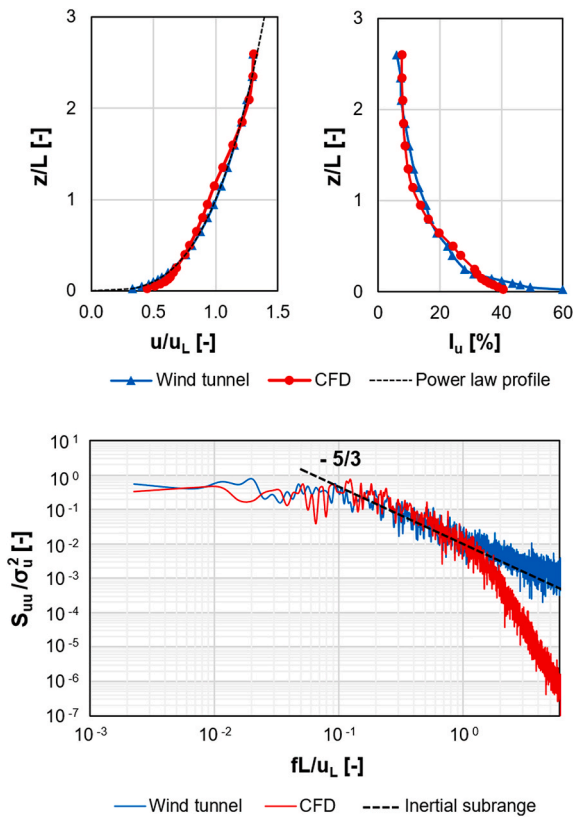


Fig. 4. Comparison of the approach flow between wind tunnel and CFD: vertical profiles of the streamwise mean velocity and the turbulence intensity, as well as the velocity power spectra at $z/L = 0.95$.

As can be seen in Fig. 3, the inlet was formed by several rectangular segments partially blocked by several circular disks in order to generate vortices. This special design was implemented in order to shorten the fetch (the flow conditioning section) of the numerical wind tunnel to maintain the highest possible spatial resolution. The segment height of the inlets is varied in proportion to the distance from the ground. The inlet velocity and the number of circular passive turbulence generators within each segment were tailored to have the best match regarding the velocity and turbulence intensity profiles of the real wind tunnel and the CFD model at the beginning of the test section (Kristóf and Papp, 2018).

Fig. 4 shows the comparison between the wind tunnel and CFD mean streamwise horizontal velocity and turbulence intensity profiles (obtained as the average of three profiles measured at $x/H = 0$, $y/H = \{-3.2, 0, 3.2\}$), along with the power-law fits on the measured velocity data set according to Eq. (1). (Averaging at 3 lateral points was only done for the CFD simulations, the experimental profiles were obtained only at $x/H = 0$, $y/H = 0$.) The coefficients of determination are $R^2 = 0.982$ and 0.927 for the mean velocity and turbulence intensity profiles, respectively. The normalized approach flow power spectra show good agreement up to the upper frequency limit defined by the mesh resolution (around $n = fL/u_L = 1.5$). For the details on the calculation of the power spectra, refer to Section 3.2.

At the ground and the surface of the cube, no-slip wall boundary conditions were used, and at the top and lateral sides of the computational domain, symmetry boundary conditions were applied. Moreover, a pressure outlet with a constant 0 Pa pressure was imposed at the end of the channel, which was used as the reference static pressure when processing the CFD results.

2.2.2. Cube model and pressure time series

In correspondence with the geometry of the wind tunnel experiments, a cube of $L = 20$ cm edge length was modeled with surface points

Table 2

Details of the mesh convergence study. (Cube edge length: $L = 20$ cm)

Mesh resolution [mm]	Cells per cube edge [-]	Total cell count (million)	Average time step size [s]	Drag coefficient [-]	
				0°	45°
7.69	26	9.13	$5.2 \cdot 10^{-4}$	1.20	0.85
8.45	24	6.88	$5.4 \cdot 10^{-4}$	1.19	0.87
9.70	21	4.55	$6.9 \cdot 10^{-4}$	1.17	0.78
13.04	15	1.88	$9.4 \cdot 10^{-4}$	1.17	0.83
37.50	5	0.079	$3.0 \cdot 10^{-3}$	1.09	0.64

for pressure data acquisition at the same locations, as shown in Fig. 2. The flow around the cube was simulated for 0° and 45° wind directions.

The numerical results were sampled for $t_{s1} = 15$ s for obtaining the mean and fluctuating pressure distributions, using the results of the 5 ... 20 s time interval (of physical time). The initialization run was performed over the first 5 s comprising 7.9 flow-through times based on the volumetric mean velocity.

The sampling frequency (i.e., the time step) of the simulation is not constant. Based on our assessment, its average is around 1900 Hz (refer to Table 2), hence, almost four times the sampling frequency of the pressure measurements from the wind tunnel experiments ($f_s = 500$ Hz). The time series were downsampled with linear interpolation to match the sampling frequency of the pressure scanner used in the wind tunnel measurements. For the spectral analysis, the acquisition time in the CFD simulations was equal to that of the experiment ($t_{s2} = t_{ac} = 120$ s). Note that using the shorter sampling interval ($t_{s1} = 15$ s) produced an average relative error of 1.1% and 4.4% compared to the longer one ($t_{s2} = 120$ s) for the mean and the fluctuating pressure coefficients, respectively.

2.2.3. Numerical setup and mesh sensitivity

The continuity and Navier-Stokes equations are solved on an equidistant Cartesian mesh, using the Finite Volume Method for discretization. Turbulence is modeled using Large Eddy Simulation, and the effect of sub-grid scale stresses is taken into account by the Smagorinsky model ($C_s = 0.1$). The wall modeling involves an algebraic approach, computing the wall shear stress from the standard law of the wall.

The diffusive terms are computed with a central differencing scheme, and the convective terms are calculated with a second order scheme with minmod limiter. The solver utilizes the fractional step approach, where the face velocities are obtained using Rhie-Chow interpolation and the solution of a pressure Poisson equation, and corrected using mass conservation principles. The time step size is set based on the Courant–Friedrichs–Lewy condition (with the Courant number being kept around 1.8), using a two-step Runge-Kutta scheme for all transport equations, along with an adaptive time step selection based on the convection time scale. The Runge-Kutta scheme itself is second order, but the face velocities for convection are frozen, so the overall order of accuracy is first order in time. It is acknowledged that the application of the minmod limiter and the first order time integration can introduce numerical dissipation, which should be minimized in LES calculations (except for the MILES approach, see Fureby and Grinstein, 1999), because the numerical dissipation damps fluctuations, see e.g., Ikegaya et al. (2019).

All algebraic systems are solved using a combination of the conjugate gradient and the algebraic multigrid methods, with agglomeration, coarsening, and smoothing, taking advantage of the structured nature of the mesh. The maximum applicable cell count of the applied equidistant Cartesian grid – the use of which is mandatory in ANSYS Discovery Live 2019R3 – is dependent on the size of the GPU's video memory (VRAM). In the present study, an Nvidia GTX 1080Ti GPU with 11 GB VRAM was used, resulting in a maximum of 9.13 million cells. The finest resolution divides the cube edge length into 26 elements. In the LES study of Gousseau et al. (2013) 20 cells per building edge were sufficient for

resolving 80% of the total turbulent kinetic energy, while a 30-cell resolution captured 91% of the total TKE around a high-rise building.

To assess the grid dependence of the CFD model, a mesh sensitivity analysis was performed, in which the total drag force (F_D) acting on the cube was monitored for both 0° and 45° wind directions using five meshes of different resolutions. The drag coefficient c_D , defined by Eq. (3), was calculated based on the velocity at half cube height ($u_{0.5L}$), taken from Eq. (1).

$$c_D = \frac{F_D}{0.5\rho u_{0.5L}^2 A_{proj}} \quad (2)$$

In the above formula, A_{proj} is the projected frontal area of the cube, the value of which is L^2 for 0° , and $\sqrt{2}L^2$ for 45° wind direction. The results of the grid sensitivity analysis – with the acquisition time being t_{SI} – are compiled in Table 2 and are shown in Fig. 5.

Since Large Eddy Simulation is applied, both the discretization error and the energy of unresolved turbulence change with the grid size (which is uniform in the entire simulation domain). The pressure coefficients computed using the finest mesh ($L/\Delta x = 26$) show a general improvement (i.e., they are significantly closer to the wind tunnel results) compared to the values obtained using the coarsest reasonable ($L/\Delta x = 15$) mesh resolution. The drag coefficient displays fluctuating convergence with the grid spacing as a consequence of mapping the cube’s surface on the equidistant numerical grids of various resolutions; that is, the discrete representation of the cube can be smaller or larger than the actual geometry. This effect is more pronounced for the 45° setup.

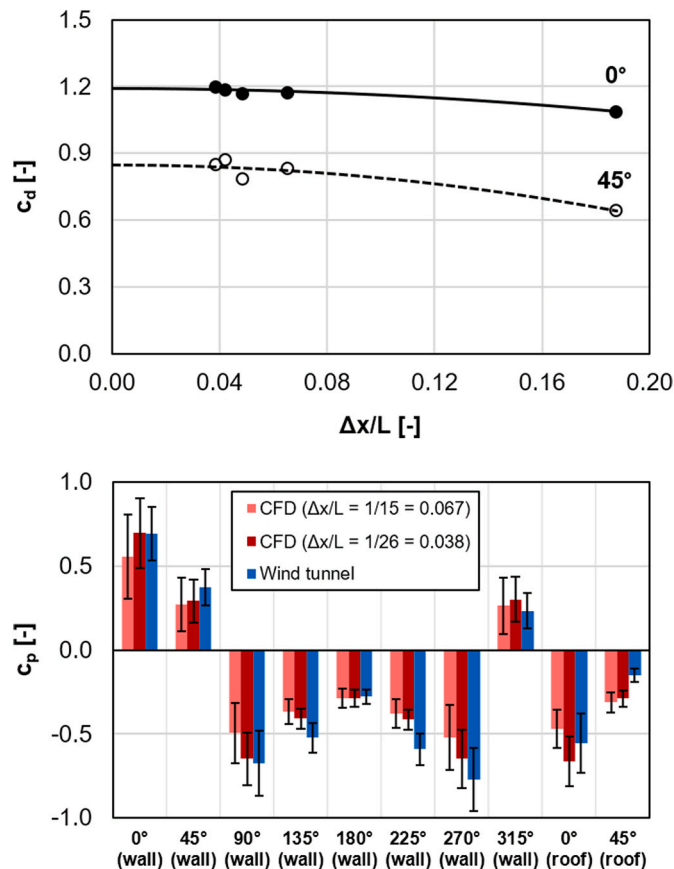


Fig. 5. Results of the grid sensitivity analysis. Top: drag coefficient of the cube, as the function of the mesh resolution relative to the cube edge length (the fitted lines are only eye-guides). Bottom: time average (solid bars) and fluctuating (error bars) pressure coefficients in the middle point (Point 18, see Fig. 2) of each face of the cube.

The simulation results presented later in Section 3 were run using the finest mesh possible with the current GPU (see Table 2). It is worth mentioning that each of these simulations needed less than six hours of computational time. For direct comparison, an LES simulation similar in geometry, cell count, and time step size was run to 1 s of physical time in ANSYS Fluent, using a 16-core Intel Xeon Silver 4110 CPU, and it was approximated that 804 hours (more than a month) would have been needed to cover the same 20 s of physical time.

3. Results and discussion

Whilst the main interest of this paper is the statistics of the flow integrated over a long time, for the sake of visual impression, two snapshots of different flow variables are displayed as well. As can be seen in Fig. 6, a horseshoe vortex is formed in front of the building model, shown by both the streamlines and the visualization of the vortex cores. The flow separation behind the front edges of the building model can also be seen in this figure, indicated by both the negative surface pressures and detached streamlines.

3.1. Surface pressure distributions

The comparison of the mean pressure coefficients (Fig. 7) reveals an overall agreement concerning their magnitudes and pattern, which implies that the dominant flow structures are captured well by the CFD model, both for 0° and 45° wind directions. This is underlined by the validation metrics presented in Table 3, which in general, reveal performance metrics close to the target values. However, some apparent

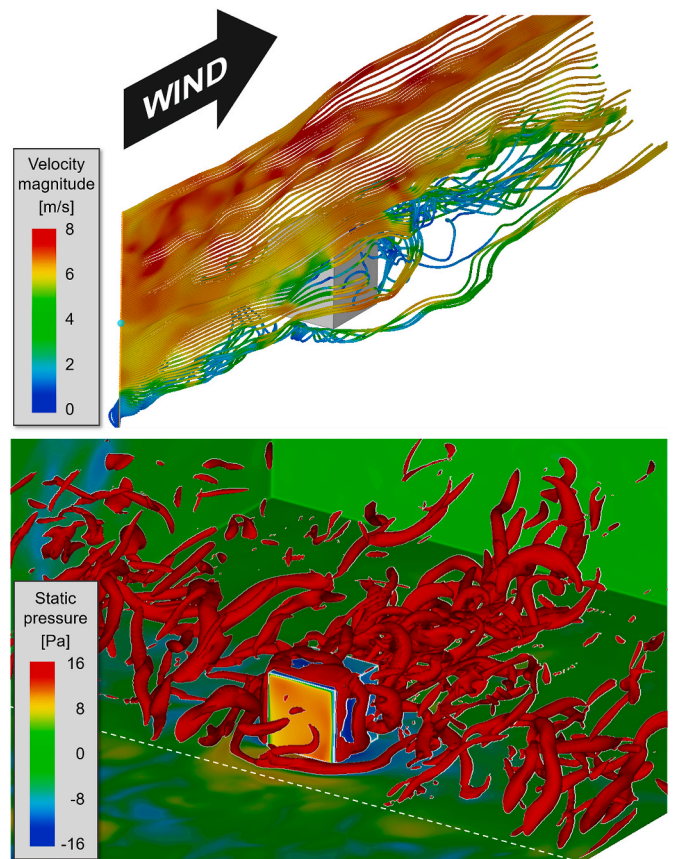


Fig. 6. Instantaneous flow variables at $t = 5$ s. Top: 3D streamlines. Bottom: static pressure distribution on the solid surfaces, combined with the iso-surfaces of the 2nd invariant of the rate of strain tensor ($\lambda_2 = -2.39 \cdot 10^3$) visualizing the vortex cores (displayed downstream of the white dashed line only).

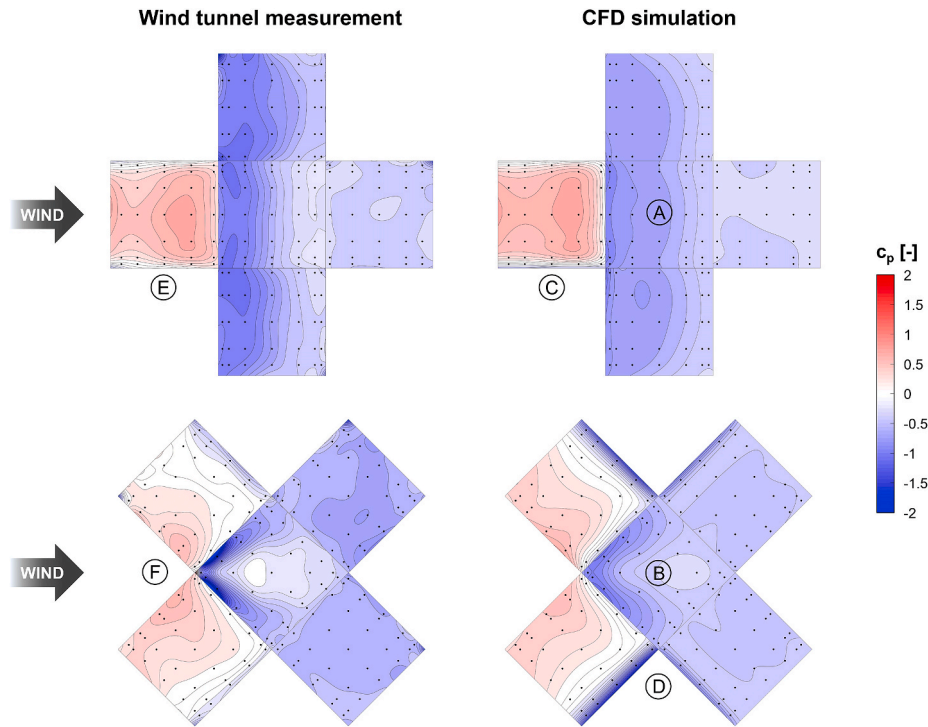


Fig. 7. Comparison of the mean pressure coefficient distributions on the surface of the cube.

deviations from the experimental results can be pointed out. Firstly, in the case of 0° wind direction, the computed pressure values of the suction zones on the top and lateral sides of the cube (A) extend over a smaller range than that of the wind tunnel measurements. These smaller gradients can be attributed to the fact that the spatial resolution, due to the equidistant grid, is not fine enough locally. Similarly, in the 45° case, the suction zone of the delta wing vortices is less intensive (B), which can be attributed to the same reason. Due to the imperfect discretization of the geometry – as a consequence of the equidistant Cartesian grid –, the numerical model displays minor asymmetries in the average pressure field (such as C) and suction areas around the lateral edges for the oblique wind direction (D). It must be noted that minor asymmetries can be observed in the case of the wind tunnel measurement as well (noticeable at the frontal faces for both wind directions – E and F) due to imperfect positioning or lateral inhomogeneity in the approach flow field.

The CFD results of the fluctuating pressure coefficient (c'_p) shown in Fig. 8 display overall agreement with the measurement data in the case of 0° wind direction, despite the minor discrepancy at the front face (G), which can be attributed to the slight differences in the approach flow profiles between the wind tunnel and the CFD model. Moreover, similarly to the mean surface pressure distribution, smaller gradients are present in the CFD model concerning the fluctuations, for example, on the top of the cube (H and I) and near the leading edge for 45° wind direction (J). It is also important that in this latter case, the pressure fluctuations caused by the delta wing vortices on the top of the cube are not reproduced to a

sufficient accuracy by the CFD model (I). Finally, similarly to the mean surface pressure distribution (c_p), the effect of the imperfect spatial discretization can also be observed around the lateral edges of the 45° angled cube, resulting in higher fluctuations than those of the wind tunnel measurements (K). It can be expected that the refinement of the equidistant mesh, which can be simply achieved by increasing the GPU VRAM capacity, could further improve the accuracy of the CFD results in terms of both the mean and fluctuating surface pressures.

The global performance metrics applied to the total 350 measurement points were calculated following the below formulas according to Chang and Hanna (2004) and Franke et al. (2007). The metrics' full names and the results are presented in Table 3.

$$R = \frac{\overline{(O_i - \bar{O}) (P_i - \bar{P})}}{\sigma_O \sigma_P} \quad (3)$$

$$FAC2 = \frac{1}{N} \sum_{i=1}^N n_i \quad \text{with} \quad (4)$$

$$n_i = \begin{cases} 1 & \text{if } 0.5 \leq \frac{P_i}{O_i} \leq 2 \\ 1 & \text{if } |O_i| \leq \Delta_a \text{ and } |P_i| \leq \Delta_a \\ 0 & \text{otherwise} \end{cases}$$

Table 3

Global validation metrics for the mean and fluctuating surface pressure coefficients: altogether, and for the different wind directions separately. (N.A.: not applicable for mixed positive and negative values according to Franke et al., 2007.)

Validation metric	c_p (all)	c_p (0°)	c_p (45°)	c'_p (all)	c'_p (0°)	c'_p (45°)	Target value
Correlation coefficient (R)	0.898	0.951	0.839	0.734	0.829	0.601	1
Factor of two of observations (FAC2)	0.920	0.943	0.897	0.983	1.000	0.966	1
Fractional bias (FB)	N.A.	N.A.	N.A.	0.055	0.024	0.095	0
Geometric mean bias (MG)	N.A.	N.A.	N.A.	0.951	1.002	0.902	1
Normalized mean square error (NMSE)	N.A.	N.A.	N.A.	0.098	0.040	0.194	0
Geometric variance (VG)	N.A.	N.A.	N.A.	1.076	1.037	1.116	1
Average absolute deviation (AAD)	0.150	0.131	0.169	0.026	0.022	0.030	0

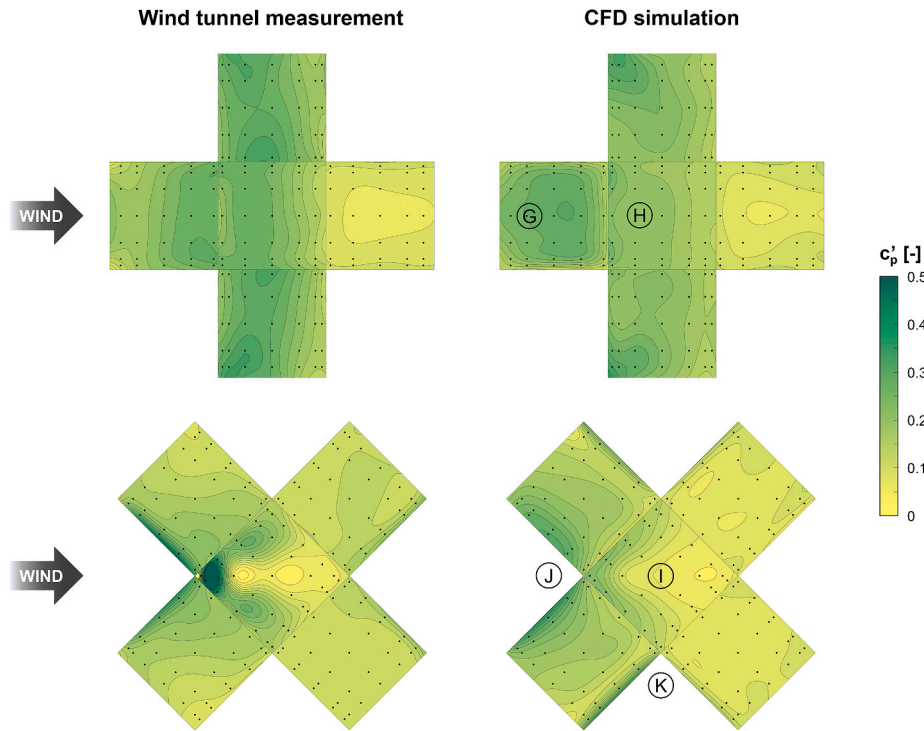


Fig. 8. Comparison of the fluctuating pressure coefficient distributions on the surface of the cube.

$$FB = \frac{\bar{O} - \bar{P}}{0.5 (\bar{O} + \bar{P})} \quad (5)$$

$$MG = \exp\left(\ln\tilde{O}_i - \ln\tilde{P}_i\right) \text{ with} \quad (6)$$

$$\tilde{O}_i = \max(O_i, \Delta_a) \text{ and } \tilde{P}_i = \max(P_i, \Delta_a)$$

$$NMSE = \frac{\overline{(O_i - P_i)^2}}{\bar{O}\bar{P}} \quad (7)$$

$$VG = \exp\left(\overline{\left(\ln\tilde{O}_i - \ln\tilde{P}_i\right)^2}\right) \text{ with} \quad (8)$$

$$\tilde{O}_i = \max(O_i, \Delta_a) \text{ and } \tilde{P}_i = \max(P_i, \Delta_a)$$

In the above equations, P_i denotes the model predictions (results of the CFD simulations), and O_i denotes the pressure coefficients observed in the wind tunnel experiments. Moreover, \bar{O} and \bar{P} stand for the averages, σ_O and σ_P represent the standard deviations, and N denotes the number of elements of the O and P data sets. The absolute and relative allowed deviations are defined as $\Delta_a = \delta_p/p_{dyn,L} = 0.142$ (based on the total measurement uncertainty) and $\Delta_r = 0.25$ (recommended by Franke et al., 2007). Remark: Δ_a is only applicable for the mean results (c_p), it is not considered for the fluctuations (c_p').

Moreover, the average absolute deviation used by Montazeri and Blocken (2013) for comparing the simulated and measured surface pressures was obtained as:

$$AAD = \overline{|O_i - P_i|} \quad (9)$$

The global validation metrics presented in Table 3 indicate good overall correspondence between the experimental and simulation results (90% and 73% correlations for c_p and c_p' , respectively), especially if the very limited computational demand of the CFD model is taken into account. Furthermore, it was found that the average absolute deviation of the mean surface pressures is similar in magnitude to the measurement uncertainty (AAD = 0.150, Δ_a = 0.142). Looking at Table 2, a clear

asymmetry can be observed between the two wind directions, as the validation metrics corresponding to the 0° case are closer to the target values than in the 45° case, reinforcing the conclusion made above: the reproduction of the surface pressure distribution is more accurate when the edges of the Cartesian grid are aligned with the geometry.

The local (pointwise) relative deviation of the CFD results from the experimental data was calculated as

$$RD_i = \frac{P_i - O_i}{O_i} \text{ if } |O_i| > T \quad (10)$$

In the above formula, the threshold T is applied to exclude excessively large relative deviations obtained purely from the division by near-zero measured values. It is important that by using this definition, the inaccuracies of the numerical model are not eliminated; only errors due to the measurement uncertainty are limited. The threshold value is $T = \Delta_a$ for the mean pressure coefficients, i.e., the points within the measurement uncertainty (30 of the total 350) are ignored. No threshold is applied to the fluctuations, i.e., all of those data are taken into account.

The metrics representation plots (scatter plots) are displayed in Fig. 9, revealing, again, that the reproduction of the surface pressure distribution is more accurate when the edges of the building model are aligned with the coordinate directions. On the histograms of the relative deviations, continuous probability density functions (with k shape, σ scale, and μ location parameters) of the so-called Generalized Extreme Value distribution were fitted using the software EasyFit. It can be observed that the magnitude of both the time average and the fluctuations of the surface pressures are underestimated both on average (mean) and most often (mode), see Table 4, along with additional statistical parameters of the PDFs.

3.2. Spectral analysis

The pressure power spectra of all the face center points (Point 18 in Fig. 2) were compared between the measurements and the simulations for two mesh sizes. The power spectral density of c_p (denoted by S_{pp}) depicted in Fig. 10 is defined as the squared absolute value of the

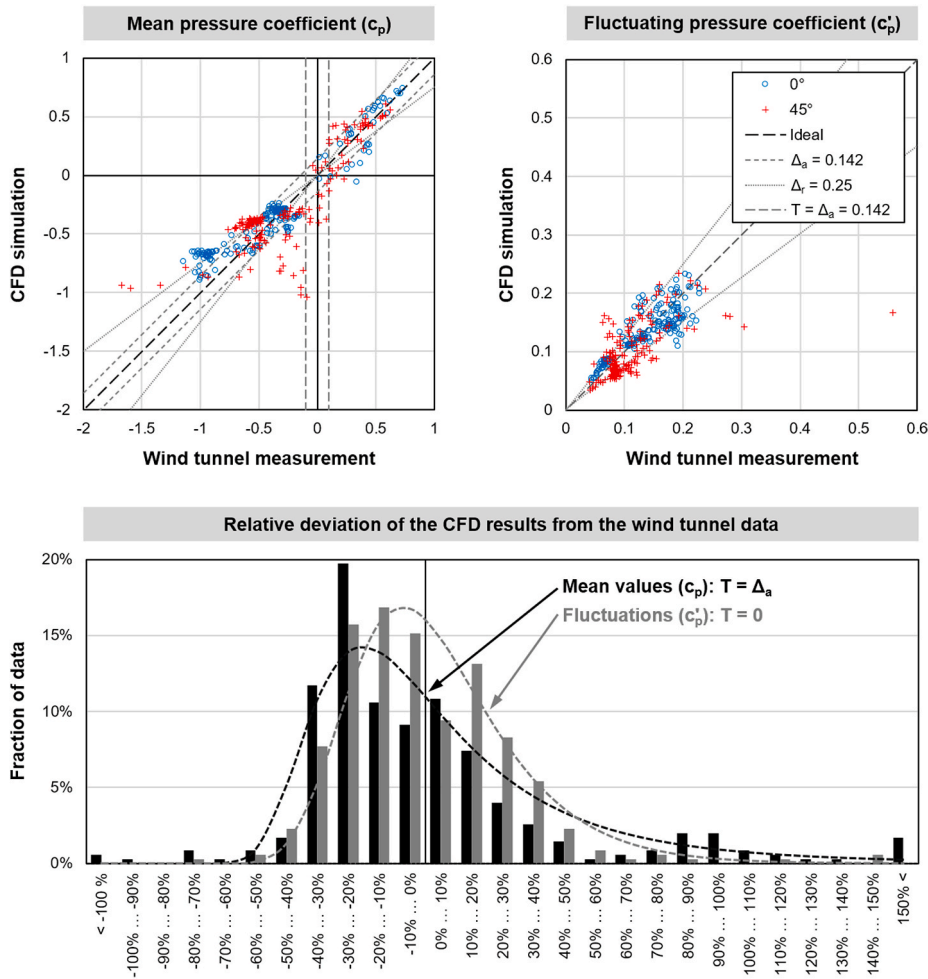


Fig. 9. Top: scatter plots of the measured and simulated mean and fluctuating pressure coefficients. The ranges of the absolute and relative measurement uncertainties as well as the threshold are marked where applicable. Bottom: histograms showing the distributions of the relative deviations of all the data points.

Table 4

Parameters of the continuous Generalized Extreme Value probability density functions fitted on the relative deviation data sets. (Data in this table represent the relative deviations of the CFD results from the experimental results in percentage.)

Data set	k	σ	μ	Mode	Mean	St. Dev.	Skewness	Kurtosis
Mean values (c_p)	0.192	26.3	-20.8	-25.5	0.659	47.8	-3.46	41.8
Fluctuations (c'_p)	-0.0387	21.8	-13.3	-12.4	-1.49	26.7	0.925	1.48

spectral components, and it is normalized by the total variance of the corresponding time series; therefore, the shape of the spectra can be directly compared. The power spectral distributions are shown as the function of the normalized frequency, a Strouhal-number-like quantity, obtained by multiplying the frequency by the ratio of the reference length and reference velocity ($n = fL/u_L$). The spectra were obtained using Fourier analysis (FFT), using a (non-overlapping) window size of 4096 points with a rectangular window function, resulting in 14 independent spectra in each of the points for averaging in order to obtain the final curves. In the log-log diagrams, a $-5/3$ slope is also displayed, which characterizes the inertial subrange of the Kolmogorov spectrum.

It can be observed in Fig. 10 that the normalized spectra of the numerical model show good agreement with those of the wind tunnel experiments up to the frequency of $n_{upper} \approx 0.55$. Small, high-frequency eddies are not resolved in the CFD model due to the finite spatial and temporal discretization, resulting in a faster decay in amplitude above n_{upper} , thus producing a shorter $-5/3$ slope compared to the wind tunnel spectra. It can also be seen that the cut-off-like behavior is present at a lower frequency

limit in the case of a coarser mesh resolution ($L/\Delta x = 15$). The dimensionless spectra generally show relatively lower energy content for the CFD simulations compared to the wind tunnel measurements at the horizontal plateau (below $n_{lower} \approx 0.05$), which can be a consequence of the larger-scale eddies not being present due to the limited size of the computational domain. It can be expected that the improvement of the numerical results, namely, widening the captured frequency range, can be accomplished by utilizing a GPU with higher VRAM capacity: by having more memory, the simulation domain can be made larger while keeping or even refining the mesh resolution.

3.3. Comparison with field measurements

The results of the present study are compared with field measurements as well. Richards and Hoxey (2012) documented the surface pressure distribution of the so-called Silsoe cube of 6 m edge length, subjected to a real atmospheric boundary layer specific to rural terrain (with a different mean velocity profile exponent of $\alpha_u = 0.17$). The mean

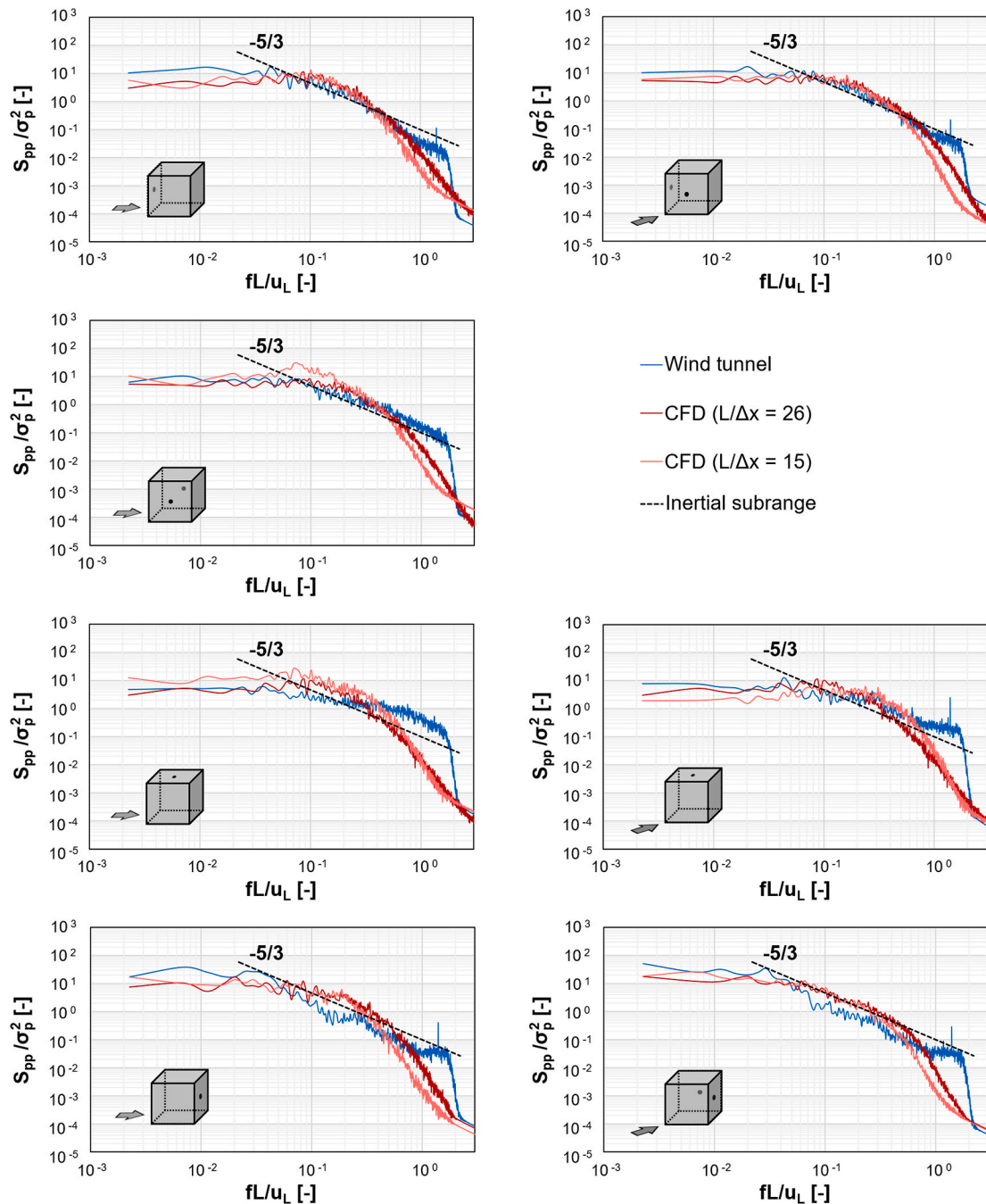


Fig. 10. Power spectral densities of the pressure coefficient on the surface of the cube for 0° (left) and 45° (right) wind directions. Locations from top to bottom: front, lateral, top, and rear faces. Spectra obtained in symmetric locations were averaged.

and the standard deviation pressure distributions of the present study as well as the field experiment are compared in Fig. 11, and Fig. 12.

Fig. 11 shows that both the wind tunnel and CFD mean pressure distributions follow the tendencies observed in the field measurements well along the so-called vertical rings. The most pronounced differences between the time-averaged results of the field and the wind tunnel measurements can be found at the roof and the lateral sides of the cube. At the top of the cube, the suction zones created by the separating vortices show lower values for both the numerical simulation and the wind tunnel measurements. These deviations could be the consequence of the differences in the approach flow profiles. At the lateral sides for 0° wind direction, the magnitude of the low-pressure zone is two times larger for both models presented in this paper compared to the Silsoe experiment. The distributions of the standard deviation pressure coefficient also show good

correspondence between the wind tunnel experiment and the CFD study, although, the wind tunnel study produces slightly larger fluctuations on the cube top and on the lateral sides.

As can be seen from the graphs of Fig. 12, the wind tunnel data show excellent correspondence with the results of the field measurements regarding the mean pressure coefficient distribution along the horizontal rings. The numerical model displays some deficiencies in replicating the measurement results in the area of high gradients, in particular, at the low-pressure regions downstream from the separation points on the lateral walls of the cube. The measured and computed standard deviation pressure coefficient distributions also show good agreement along the horizontal rings. In the CFD model, the high negative pressures and intense fluctuations near the lateral edges of the 45° angled cube are also shown; furthermore, the mean pressure values

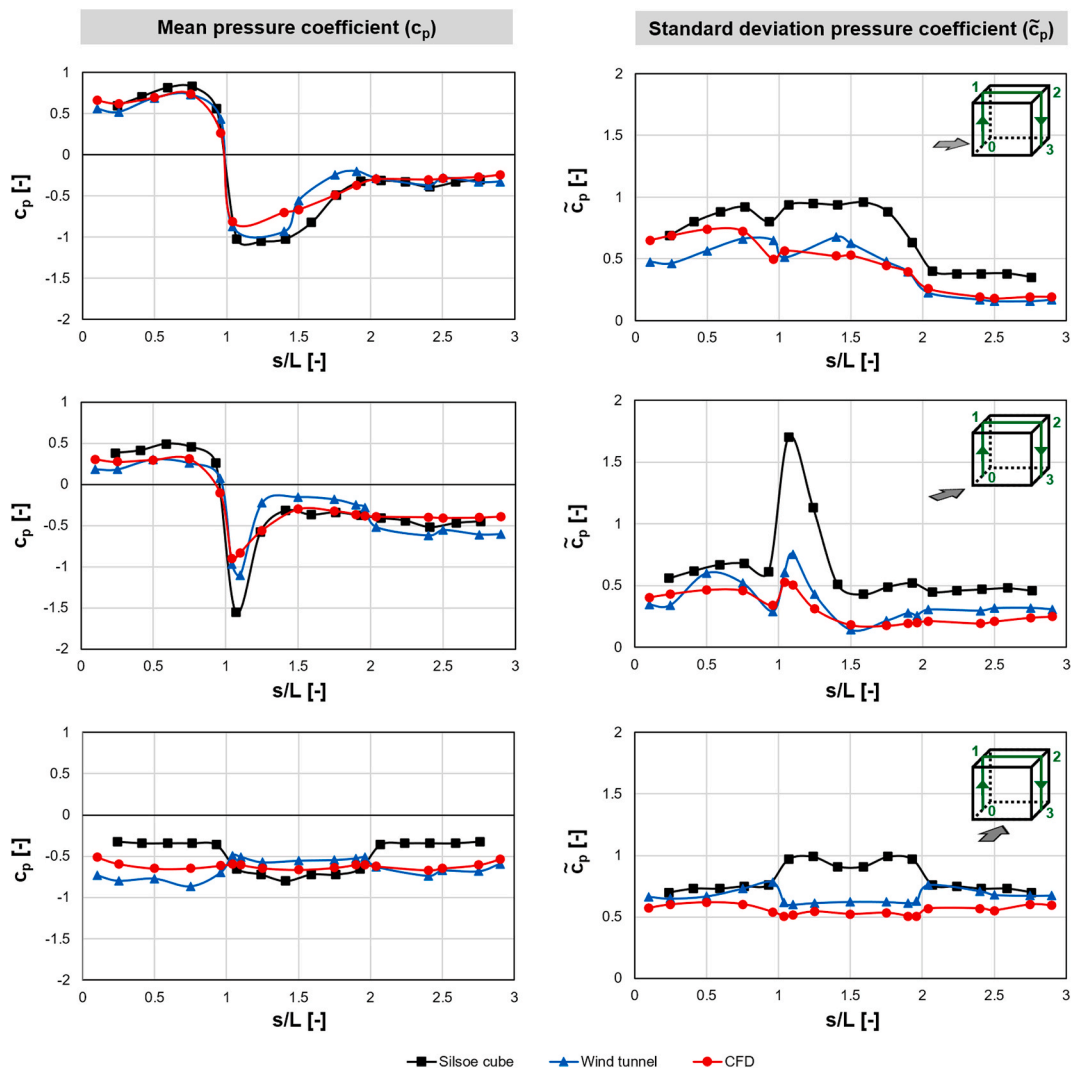


Fig. 11. Comparison of the mean (left) and standard deviation (right) pressure coefficients obtained on the surface of the Silsoe cube, in the wind tunnel experiment, and in the CFD simulation along the vertical rings.

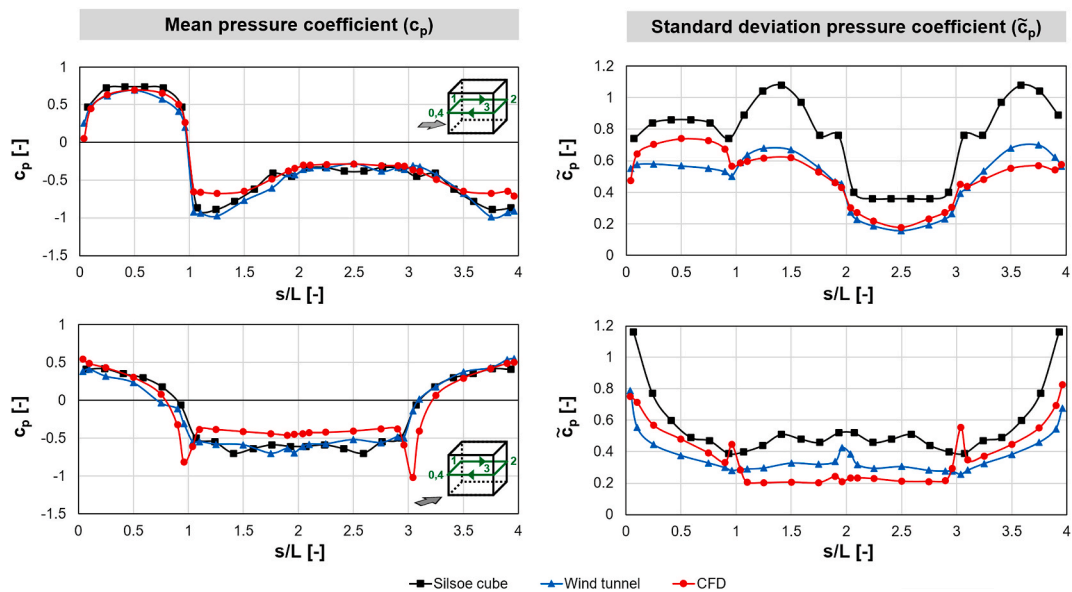


Fig. 12. Comparison of the mean (left) and standard deviation (right) pressure coefficients obtained on the surface of the Silsoe cube, in the wind tunnel experiment, and in the CFD simulation along the horizontal rings.

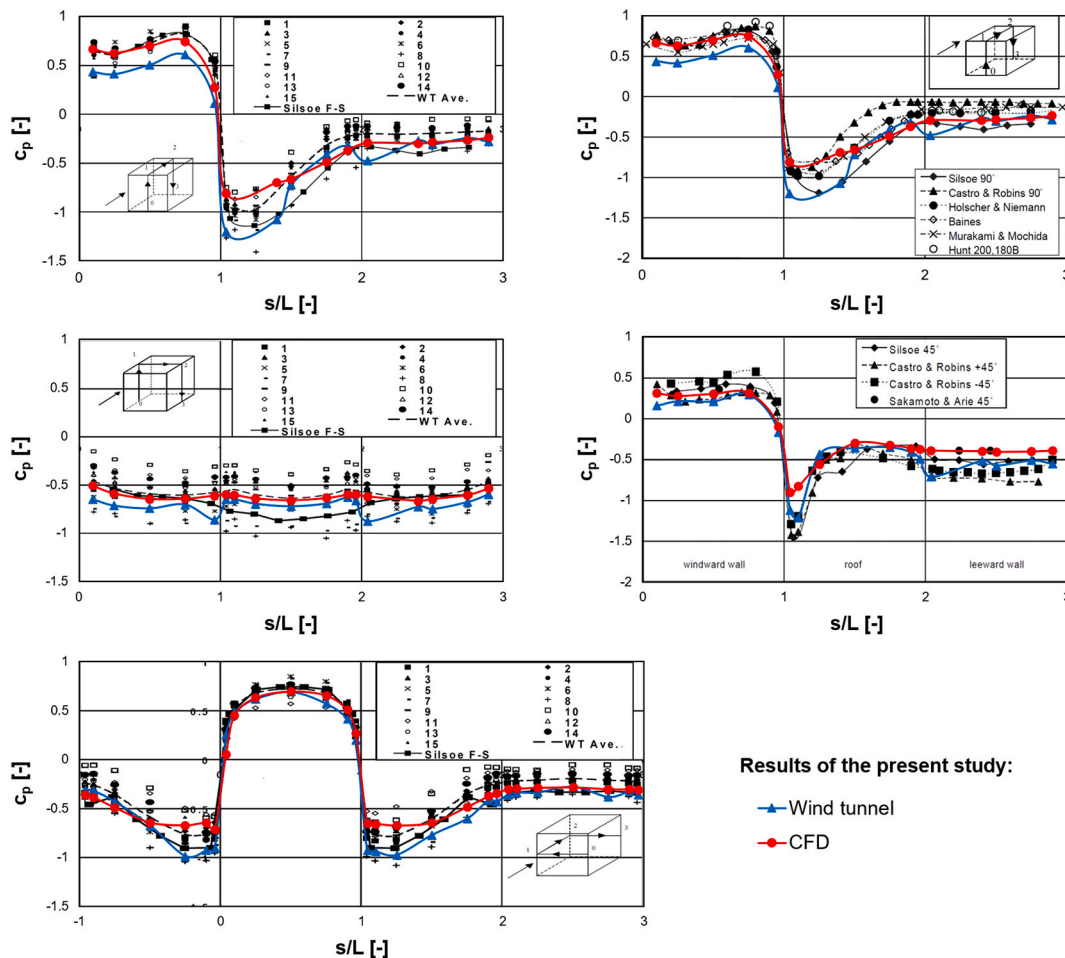


Fig. 13. Comparison of the mean surface pressure distributions: CFD results (red), wind tunnel results presented in this study (blue) and data from previous experiments (black). Original images by Richards et al. (2001), in which the wind tunnel results of Holscher and Niemann (1998) are shown on the left-hand side. Reproduced with permission from Elsevier.

are slightly more moderate at the rear sides compared to the wind tunnel and full-scale results.

Compared to the field experiments, the standard deviation pressure coefficients of the present study show correct tendencies; however, a noticeable deficit is present along both the vertical and horizontal rings (Figs. 11 and 12, respectively), which can also be caused by the different approach flow characteristics.

3.4. Comparison with other wind tunnel experiments

The results of the present study were compared to previous wind tunnel measurements as well. Richards et al. (2001) compiled results from wind tunnel studies, including measurements obtained in various boundary layer wind tunnels, with very similar characteristic exponents of the mean velocity profile $\alpha_u = 0.22 \pm 0.02$ (Holscher and Niemann, 1998). The comparison presented in Fig. 13 highlights that the mean pressure coefficient distribution on the surface of the cube is rather sensitive to the properties of the atmospheric boundary layer, especially to the turbulence profiles, which were different in the investigated cases. However, it can be seen that the CFD results of the present study fall into the range of the previously measured pressure distributions. Hence, deviations between the CFD results and the wind tunnel data of the present study may also be attributed to minor differences of the approach flow characteristics.

4. Conclusions and outlook

For the determination of dynamic wind load on buildings caused by atmospheric flow and turbulence, the application of scale resolving turbulence models, such as Large Eddy Simulation is preferable over Reynolds-averaged turbulence models. When using conventional CFD models running on CPU, the calculation takes a significant amount of time, suboptimal for the engineering practice: the process typically lasts for weeks. The present numerical model was created in ANSYS Discovery Live 2019R3, which utilizes effective parallel computing on a standard desktop PC equipped with a single CUDA-compatible GPU, which can produce statistically converged LES results in about six hours of computational time using nine million cells. For direct comparison, a similar LES calculation needs approximately 804 hours to complete using a 16-core CPU.

Due to the use of an equidistant Cartesian grid applied in ANSYS Discovery Live 2019R3, the location of the boundary layer separation on curved surfaces may be inadequately predicted by the CFD model. However, for cuboid buildings with sharp contours, the separation point is pre-defined, and the local boundary layer evolution is not relevant for the surface pressure distribution. Another source of inaccuracy is the difference between the real geometry and its representation by the equidistant mesh in the CFD model. The coarse geometrical representation caused non-monotonous convergence of the drag force on meshes of increasing resolution. This error comes more into effect if surfaces are oriented oblique to the approach wind instead of parallel and perpendicular, as evidenced for the 0° and 45° wind directions investigated

herein. In the latest release (ANSYS Discovery 2021R2, at the time of publication), however, a boundary-fitted mesh is available using the immersed boundary method (Ye et al., 1999), promising more accurate results for bluff bodies with oblique walls and for flows over curved surfaces.

To validate the numerical model, the time average of the pressure distribution on the surface of a cube-shaped building model along with the pressure fluctuations were compared with the results of wind tunnel measurements on the entire cube surface for 0° and 45° wind directions. The CFD model showed to reproduce the relevant mean and time-dependent flow structures and pressure field features. The most considerable deviations were found at those locations where large gradients were present, typically in the separation zones behind the lateral and upper edges of the frontal surface, which led to the underestimation of the local pressure minima.

Compared to the measured values, the power spectra of the CFD pressure fluctuations showed a good agreement in the intermediate frequency range, where the turbulent scales are properly resolved by the numerical model, above the dimensionless frequency threshold ($n \approx 0.05$) defined by the size of the computational domain. The dimensionless cut-off frequency corresponding to the upper frequency limit related to the mesh size was in the range of $n \approx 0.55$ in the examined cases.

Despite the deviations mentioned above, the accuracy of the calculated mean and fluctuating surface pressure distributions can be acceptable for many engineering applications. The correlation coefficients for the mean and fluctuating surface pressures between the experimental and simulation data were 0.90 and 0.73, in the case of the finest discretization ($L/\Delta x = 26$) allowed by an Nvidia GTX 1080Ti GPU with 11 GB on-board graphical memory (VRAM). Each of the errors noted above may be reduced by increasing the mesh resolution and the domain size, which can be achieved simply by using a GPU with higher video memory capacity. Note that the performance of video cards is rapidly increasing: the most powerful CUDA-based GPUs feature up to 48 GB of VRAM at the time of the publication.

Our model results were also compared with the Silsoe full-scale field experiment (Richards and Hoxey, 2012). In terms of the mean pressure coefficients, the CFD and wind tunnel data approached the results of the field measurements with good accuracy, while the standard deviation pressure coefficient distributions of the present study also showed correct tendencies compared to the full-scale experiment. It was also demonstrated that both the experimental and the CFD results shown in this paper were in line with previous wind tunnel results (Hölscher and Niemann, 1998; Richards et al., 2001).

In conclusion, the continuing advancement of the presented GPU-based numerical model is a promising development for effectively estimating the dynamic wind loads on buildings and identifying design problems fast enough for the engineering practice without accessing high-performance computing.

Data availability statement

Some or all data, models, or code that support the findings of this study are available from the corresponding author upon reasonable request. (Measurement and simulation results, CFD model.)

CRediT authorship contribution statement

Bálint Papp: Methodology, Software, Validation, Formal analysis, Investigation, Writing – original draft, Writing – review & editing, Visualization, Funding acquisition. **Gergely Kristóf:** Conceptualization, Writing – original draft, Writing – review & editing, Supervision, Project administration, Funding acquisition. **Christof Gromke:** Methodology, Validation, Investigation, Data curation, Writing – original draft, Writing – review & editing.

Declaration of competing interest

The authors declare that they have no known competing financial interests or personal relationships that could have appeared to influence the work reported in this paper.

Acknowledgements

This study was funded by grant no. K 124439, NKFIH from the National Research, Development, and Innovation Office, Hungary. The research reported in this paper and carried out at the Budapest University of Technology and Economics has been supported by the National Research Development and Innovation Fund (TKP2020 National Challenges Subprogram, Grant No. BME-NCS and TKP2020 Institution Excellence Subprogram, Grant No. BME-IE-WAT) based on the charter of bolster issued by the National Research Development and Innovation Office under the auspices of the Ministry for Innovation and Technology. The Ostpartnerschaften program from the German Academic Exchange Service (DAAD) is acknowledged for helping to initiate the collaboration. Bálint Papp's contribution to this paper was supported by the ÚNKP-19-2 New National Excellence Program of the Ministry for Innovation and Technology; and the Gedeon Richter Talent Foundation (registered office: Gyömrői út 19-21, 1103 Budapest, Hungary), established by Gedeon Richter Plc., within the framework of the Gedeon Richter PhD Scholarship. The authors acknowledge the support of CFD.HU Ltd. in providing access to the necessary hardware and software, as well as express their gratitude towards Dipankar Choudhury (Vice President, Research) and Justin Hendrickson (Director of Product Management) of ANSYS, Inc. for providing insight to the simulation methods applied in ANSYS Discovery Live.

References

- Aboshosha, H., Elshaer, A., Bitsuamlak, G.T., El Damatty, A., 2015. Consistent inflow turbulence generator for LES evaluation of wind-induced responses for tall buildings. *J. Wind Eng. Ind. Aerod.* 142, 198–216.
- Balogh, M., Parente, A., Benocci, C., 2012. RANS simulation of ABL flow over complex terrains applying an Enhanced k-ε model and wall function formulation: implementation and comparison for fluent and OpenFOAM. *J. Wind Eng. Ind. Aerod.* 104, 360–368.
- Bergh, H., Tijdeman, H., 1965. Theoretical and experimental results for the dynamic response of pressure measuring systems. National Lucht- en Ruimtevaartlaboratorium (NL), report number: NLR-TR F.238, p. 51.
- Blocken, B., Stathopoulos, T., Carmeliet, J., 2007. CFD simulation of the atmospheric boundary layer: wall function problems. *Atmos. Environ.* 41 (2), 238–252.
- Blocken, B., 2014. 50 years of computational wind engineering: past, present and future. *J. Wind Eng. Ind. Aerod.* 129, 69–102.
- Blocken, B., 2015. Computational Fluid Dynamics for urban physics: importance, scales, possibilities, limitations and ten tips and tricks towards accurate and reliable simulations. *Build. Environ.* 91, 219–245.
- Blocken, B., 2018. LES over RANS in building simulation for outdoor and indoor applications: a foregone conclusion? *Building Simulation* 11 (5), 821–870 (Springer Berlin Heidelberg).
- Chang, J.C., Hanna, S.R., 2004. Air quality model performance evaluation. *Meteorol. Atmos. Phys.* 87 (1–3), 167–196.
- Corrigan, A., Camelli, F.F., Löhner, R., Wallin, J., 2011. Running unstructured grid-based CFD solvers on modern graphics hardware. *Int. J. Numer. Methods Fluid.* 66 (2), 221–229.
- Dagnew, A.K., Bitsuamlak, G.T., 2014. Computational evaluation of wind loads on a standard tall building using LES. *Wind Struct.* 18 (5), 567–598.
- Din EN 1991-1-4, 2010. Eurocode 1: Actions on Structures – Part 1-4: General Actions – Wind Actions. Beuth Verlag, Berlin, p. 153.
- Din EN 1991-1-4/NA, 2010. National Annex – Nationally Determined Parameters – Eurocode 1: Actions on Structures – Part 1-4 General Actions – Wind Actions. Beuth Verlag, Berlin, p. 41.
- Domaneschi, M., Martinelli, L., Po, E., 2015. Control of wind buffeting vibrations in a suspension bridge by TMD: hybridization and robustness issues. *Comput. Struct.* 155, 3–17.
- Elsen, E., LeGresley, P., Darve, E., 2008. Large calculation of the flow over a hypersonic vehicle using a GPU. *J. Comput. Phys.* 227 (24), 10148–10161.
- EN 1991-1-4, 2005. Eurocode 1: Actions on Structures – Part 1-4: General Actions – Wind Actions. British Standards Institution, London, p. 10. Section 1.5.
- Franke, J., Hellsten, A., Schlünzen, H., Carissimo, B. (Eds.), 2007. Best Practice Guideline for the CFD Simulation of Flows in the Urban Environment, COST Action 732. COST Office, Brussels, ISBN 3-00-018312-4.

- Fureby, C., Grinstein, F.F., 1999. Monotonically integrated large eddy simulation of free shear flows. *AIAA J.* 37 (5), 544–556.
- Gousseau, P., Blocken, B., Van Heijst, G.J.F., 2013. Quality assessment of large-eddy simulation of wind flow around a high-rise building: validation and solution verification. *Comput. Fluids* 79, 120–133.
- Gromke, C., Ruck, B., 2005. Die simulation atmosphärischer grenzsichten in windkanälen. Proceedings 13th GALA fachtagung lasermethoden in der Strömungsmechanik, 51-1-51-8. German Association for Laser Anemometry.
- Gromke, C., 2018. Wind tunnel model of the forest and its Reynolds number sensitivity. *J. Wind Eng. Ind. Aerod.* 175, 53–64.
- Hölscher, N., Niemann, H.J., 1998. Towards quality assurance for wind tunnel tests: a comparative testing program of the Windtechnologische Gesellschaft. *J. Wind Eng. Ind. Aerod.* 74, 599–608.
- Huang, B.C., Leung, A.Y.T., Lam, K.M., Cheung, Y.K., 1996. Analytical determination of equivalent modal damping ratios of a composite tower in wind-induced vibrations. *Comput. Struct.* 59 (2), 311–316.
- Ikegaya, N., Okaze, T., Kikumoto, H., Imano, M., Ono, H., Tominaga, Y., 2019. Effect of the numerical viscosity on reproduction of mean and turbulent flow fields in the case of a 1: 1: 2 single block model. *J. Wind Eng. Ind. Aerod.* 191, 279–296.
- Kataoka, H., Mizuno, M., 2002. Numerical flow computation around aeroelastic 3D square cylinder using inflow turbulence. *Wind Struct.* 5 (2_3_4), 379–392.
- Keyhan, H., McClure, G., Habashi, W.G., 2013. Dynamic analysis of an overhead transmission line subject to gusty wind loading predicted by wind-conductor interaction. *Comput. Struct.* 122, 135–144.
- Kim, Y., Castro, I.P., Xie, Z.T., 2013. Divergence-free turbulence inflow conditions for large-eddy simulations with incompressible flow solvers. *Comput. Fluids* 84, 56–68.
- King, M.F., Khan, A., Delbosc, N., Gough, H.L., Halios, C., Barlow, J.F., Noakes, C.J., 2017. Modelling urban airflow and natural ventilation using a GPU-based lattice-Boltzmann method. *Build. Environ.* 125, 273–284.
- Költzsch, K., Ihlenfeld, H., Brechling, J., 1997. Einfluss des Modellierungsmaßstabes bei der Ermittlung von Windlastannahmen in Grenzschichtwindkanälen, in: Baukonstruktionen unter Windeinwirkung, WTG-Berichte Nr. 5. Windtechnologische Gesellschaft, Aachen, p. 18.
- Kristóf, G., Papp, B., 2018. Application of GPU-based large eddy simulation in urban dispersion studies. *Atmosphere* 9 (11), 442.
- Lamberti, G., Gori, C., 2020. Sensitivity of LES predictions of wind loading on a high-rise building to the inflow boundary condition. *J. Wind Eng. Ind. Aerod.* 206, 104370.
- Lim, H.C., Thomas, T.G., Castro, I.P., 2009. Flow around a cube in a turbulent boundary layer: LES and experiment. *J. Wind Eng. Ind. Aerod.* 97 (2), 96–109.
- Lund, T.S., Wu, X., Squires, K.D., 1998. Generation of turbulent inflow data for spatially-developing boundary layer simulations. *J. Comput. Phys.* 140 (2), 233–258.
- Menter, F.R., 2012. Best practice: scale-resolving simulations in ANSYS CFD. ANSYS Germany GmbH 1.
- Montazeri, H., Blocken, B., 2013. CFD simulation of wind-induced pressure coefficients on buildings with and without balconies: validation and sensitivity analysis. *Build. Environ.* 60, 137–149.
- Nozawa, K., Tamura, T., 2002. Large eddy simulation of the flow around a low-rise building immersed in a rough-wall turbulent boundary layer. *J. Wind Eng. Ind. Aerod.* 90 (10), 1151–1162.
- Onodera, N., Aoki, T., Shimokawabe, T., Kobayashi, H., 2013. Large-scale LES wind simulation using lattice Boltzmann method for a 10 km × 10 km area in metropolitan Tokyo. *Tsubame ESJ* 9, 2–8.
- Owens, J.D., Luebke, D., Govindaraju, N., Harris, M., Krüger, J., Lefohn, A.E., Purcell, T. J., 2007. A survey of general-purpose computation on graphics hardware. *Comput. Graph. Forum* 26 (1), 80–113. Oxford, UK: Blackwell Publishing Ltd.
- Patruno, L., Ricci, M., De Miranda, S., Ubertini, F., 2016. Numerical simulation of a 5: 1 rectangular cylinder at non-null angles of attack. *J. Wind Eng. Ind. Aerod.* 151, 146–157.
- Phillips, E., Zhang, Y., Davis, R., Owens, J., 2009. Rapid aerodynamic performance prediction on a cluster of graphics processing units. In 47th AIAA Aerospace Sciences Meeting Including The New Horizons Forum and Aerospace Exposition 565.
- Qu, W.L., Chen, Z.H., Xu, Y.L., 2001. Dynamic analysis of wind-excited truss tower with friction dampers. *Comput. Struct.* 79 (32), 2817–2831.
- Ricci, M., Patruno, L., Kalkman, I., de Miranda, S., Blocken, B., 2018. Towards LES as a design tool: wind loads assessment on a high-rise building. *J. Wind Eng. Ind. Aerod.* 180, 1–18.
- Richards, P.J., Hoxey, R.P., Short, L.J., 2001. Wind pressures on a 6 m cube. *J. Wind Eng. Ind. Aerod.* 89 (14–15), 1553–1564.
- Richards, P.J., Hoxey, R.P., 1993. Appropriate boundary conditions for computational wind engineering models using the k-ε turbulence model. *J. Wind Eng. Ind. Aerod.* 46, 145–153.
- Richards, P.J., Hoxey, R.P., 2012. Pressures on a cubic building—Part 1: full-scale results. *J. Wind Eng. Ind. Aerod.* 102, 72–86.
- Richards, P.J., Norris, S.E., 2011. Appropriate boundary conditions for computational wind engineering models revisited. *J. Wind Eng. Ind. Aerod.* 99 (4), 257–266.
- Schalkwijk, J., Griffith, E.J., Post, F.H., Jonker, H.J., 2012. High-performance simulations of turbulent clouds on a desktop PC: exploiting the GPU. *Bull. Am. Meteorol. Soc.* 93 (3), 307–314.
- Spalart, P.R., Leonard, A., 1987. Direct numerical simulation of equilibrium turbulent boundary layers. In: *Turbulent Shear Flows 5*. Springer, Berlin, Heidelberg, pp. 234–252.
- Tamura, T., 2009. Large eddy simulation on building aerodynamics. In: Proceedings of the Seventh Asia-Pacific Conference on Wind Engineering, pp. 131–157.
- Tamura, T., Nozawa, K., Kondo, K., 2008. AIJ guide for numerical prediction of wind loads on buildings. *J. Wind Eng. Ind. Aerod.* 96 (10–11), 1974–1984.
- Thibault, J., Senocak, I., 2009. CUDA implementation of a Navier-Stokes solver on multi-GPU desktop platforms for incompressible flows. In 47th AIAA aerospace sciences meeting including the new horizons forum and aerospace exposition 758.
- Thordal, M.S., Bennetsen, J.C., Koss, H.H.H., 2019. Review for practical application of CFD for the determination of wind load on high-rise buildings. *J. Wind Eng. Ind. Aerod.* 186, 155–168.
- Tominaga, Y., Mochida, A., Yoshie, R., Kataoka, H., Nozu, T., Yoshikawa, M., Shirasawa, T., 2008. AIJ guidelines for practical applications of CFD to pedestrian wind environment around buildings. *J. Wind Eng. Ind. Aerod.* 96 (10–11), 1749–1761.
- VDI 3783-12, 2000. Environmental Meteorology – Physical Modelling of Flow and Dispersion Processes in the Atmospheric Boundary Layer – Applications of Wind Tunnels. Beuth Verlag, Berlin, p. 36.
- Xia, H., Guo, W.W., Zhang, N., Sun, G.J., 2008. Dynamic analysis of a train-bridge system under wind action. *Comput. Struct.* 86 (19–20), 1845–1855.
- Xie, Z.T., Castro, I.P., 2008. Efficient generation of inflow conditions for large eddy simulation of street-scale flows. *Flow, Turbul. Combust.* 81 (3), 449–470.
- Ye, T., Mittal, R., Udaykumar, H.S., Shyy, W., 1999. An accurate Cartesian grid method for viscous incompressible flows with complex immersed boundaries. *J. Comput. Phys.* 156 (2), 209–240.